Engineering Solid Mechanics12 (2024) 333-342

Contents lists available at GrowingScience

Engineering Solid Mechanics

homepage: www.GrowingScience.com/esm

Optimization of laser welded ASTM A36 mild steel with different laser beam oscillation patterns utilizing experimental and simulation data

Said Ouamer [a], Karim Bensalem[a], Asim Iltaf[a*], Noureddine Barka[a] and Shayan Dehghan[a*]

[a] *Department of Mathematics, Computer Science and Engineering, University of Quebec at Rimouski, Rimouski, QC G5L 3A1, Quebec, Canada*

ARTICLEINFO

Article history:
Received 17 August 2023
Accepted 6 November 2023
Available online
6 November 2023

Keywords:
Laser Welding
ASTM A36 mild steel
Optimization
ANOVA
Taguchi

ABSTRACT

Recently, there has been an increase in the use of laser beam welding of mild steel in various industries, including petroleum refineries, power plants, pharmaceuticals, and even residential areas. This research paper focuses on studying the effects of laser welding process parameters, such as laser power and welding speed, on the tensile strength of welds. To do this, three types of laser beam oscillations (sinusoidal path, triangular path, and square path) were performed to weld 125mm x 60 and 1.8 thick sheets of ASTM A36 mild steel alloy. The researchers used statistical tools such as ANOVA to generate mathematical models and experimental designs using the Taguchi method. The results indicate that the optimal welded joint has good mechanical properties after laser welding. For ASTM A36 mild steel, the optimal parameters for laser welding are a laser power of 1800 W, a welding speed of 50 mm/s, and triangular welding mode.

1. Introduction

Laser welding's high energy density and low heat input are beneficial for producing welds with fine grains and a narrow heat-affected zone (HAZ) (Cao et al., 2022; Derevyagina et al., 2020). As a result of recrystallization during laser welding, HAZ grains can be refined (Kumar et al., 2018). Aluminium alloys, steel, and other dissimilar materials are now welded using this high-power density welding method (Yang et al., 2022). It is possible that, depending on the welding conditions and process parameters, the joints formed using this welding method will exhibit defects, such as fractures generated in the narrow-welded region (Wang, 2019). The strength of the weld and the durability of the structure are both affected by the location and magnitude of these fractures. The laser power, welding speed, defocusing distance, and shielding gas type most significantly affects the fluid and heat flows in the molten pool during laser welding (Cheng et al., 2021; Geng et al., 2019; Pankaj et al., 2019).

Mild steel's low carbon and alloying element content means it has a lower tensile strength than austenitic steel. Because of its inexpensive cost and wide range of useful applications (including automobile body panels, food cans, metal chains, wire ropes, engine components, bicycle rims, and nails and screws), it has surpassed other types of steel to become the industry standard (Karakizis et al., 2019; Prabakaran et al., 2019; Satpal et al., 2020; Wang et al., 2016). Using filler wire, Cam et al. (Çam et al., 2013) welded austenitic stainless steel 1.4404 (X2CrNiMo 18 10) and ferritic steel (grades St 37 and St 52) with a CO_2 laser. They noticed that the microstructure of welded C-Mn steels had substantial proportions of bainite/martensite in the weld zone, resulting in increased hardness in the weld areas of ferritic similar and ferritic-austenitic dissimilar joints. Ancona et al. (Ancona et al., 2007) performed the 2.5 kW laser beam butt welding on 3-mm thick aluminium–magnesium alloy 5083 specimens using helium as a shielding gas. The influence of welding speed and laser power on the tensile characteristics, hardness profiles, and porosity of butt welds was examined. At 2500 W laser power and 100 mm/s welding speed, they obtained a maximum tensile strength of 90% of the base metal. Mingsheng et al. (Xia et al., 2008) studied the metallurgical and mechanical properties of Si and Al-TRIP steel sheets welded by a diode laser Nuvonyx ISL-4000. At a rate

* Corresponding author.
E-mail addresses: asim.iltaf@uqar.ca (A. Iltaf) shayan.dehghan@uqar.ca (S. Dehghan)

ISSN 2291-8752 (Online) - ISSN 2291-8744 (Print)

doi: 10.5267/j.esm.2024.1.001

of 30 L/min, 30 l/min of Argon was employed as a shielding gas. They noticed that the fusion zone of Si-alloyed steel included martensite, whereas Al-alloyed steel had two forms of morphology, including skeletal ferrite, bainitic ferrite, martensite, and preserved austenite. In addition, they reported that the Si-alloyed TRIP steel had superior strength and ductility compared to the Al-alloyed TRIP steel. Benyounis et al. (Benyounis et al., 2008) performed the 1.5 kW CO_2 laser welding on 3 mm thick cold-rolled AISI 304 steel sheets with a constant flow rate of 5 L/min of argon shielding gas. They discovered that laser power between 1.2 kW and 1.23 kW was optimal for producing joints of high quality. El-Batahgy et al. (El-Batahgy et al., 2011) performed laser welding on duplex stainless steel with a thickness of 6.40 mm to assess the effect of process parameters on the microstructure of the fusion zone, mechanical properties, and corrosion resistance of welded joints. They discovered that the ferrite–austenite transition in the fusion zone of welded specimens is substantially influenced by the cooling rate, which is a function of laser power and welding speed. Gao et al. (Gao et al., 2008) performed laser–MIG hybrid welding on 7 mm thick mild steel plates with a 5 kW CO2 laser and a 350A conventional DCEP MIG welder. Due to the synergistic interaction of laser and arc, they noticed the "wine-cup"-shaped weld zone. In comparison to the arc zone, the laser zone had a finer grain size, higher microhardness, smaller element content in the fusion zone, and a narrower HAZ. Bhadra et al. (Bhadra et al., 2019) developed a 3D computational model utilizing the finite element approach to predict the CO2 laser weld-induced transient thermal history, residual stresses, and residual deformation in AISI 304 Steel Thin Plates. This model incorporates the influence of weld bead geometry. They noticed that the peak temperature, fusion zone (FZ), and heat-affected zone (HAZ) increased when laser power and laser welding speed decreased. Zhang et al. (Zhang et al., 2014) utilised a 10-kW high-power fibre laser to perform deep penetration laser welding on 12 mm thick stainless-steel plates. They noticed a critical region of the welding speed for complete penetration welding of thick plates with the focus point below the surface of the specimen. In addition, they found that the focus position has a significant impact on the results of high-power fibre laser welding of thick plates.

After analyzing the available literature, it was discovered that there are only a limited number of publications on laser welding of A36 mild steel. In this regard, this study focused on joining thin sheets of A36 mild steel by laser welding using various beam oscillations such as square, sinusoidal, and triangular. The mechanical properties were evaluated by analyzing the effects of laser welding process parameters, including laser power and welding speed while maintaining a constant stand-off distance. The findings of this study are expected to contribute in-depth knowledge regarding the laser welding of ASTM A36 mild steel with different laser beam oscillation patterns and improve the quality of the welding process.

2. Experimental Procedures

2.1 Properties of ASTM A36 steel

The material used for the welding experiment was ASTM A36 mild steel. Two 1.8 mm thick base metal sheets of size 60mm×40mm were welded in a butt joint configuration using an Nd: YAG laser (λ = 1070 nm) in continuous mode with the chemical composition and physical characteristics in **Table 1** and **Table 2**, respectively.

Table 1. Chemical composition of ASTM A36 mild steel

Element	Fe	C	Mn	P	S	Si	Cu
Percent	98.11	0.29	1.03	0.039	0.05	0.28	0.2

Table 2. Mechanical properties of ASTM A36 mild steel

Tensile strength (MPa)	Yield strength (MPa)	Modulus of elasticity (GPa)	Elongation (%)	Hardness (HV)
400–550	250–290	190–200	20–23	124–160

2.2 The laser welding system

The entire welding process was performed using a fiber laser source (IPG YLS-3000 with a maximum power of 3kW) and a galvanometric scanner (ILV DC-scan with a maximum amplitude of 0. 7mm to 15 mm).

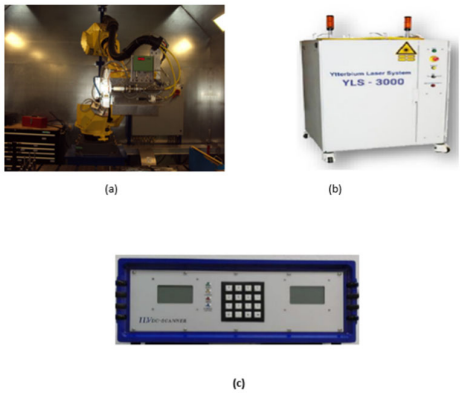

Fig. 1. (a) Fanuc®M-710iC robot and HIGHYAG BIMO laser head (b) YLS-3000 laser source (c) ILV DC-scan

A six-axis system (Fanuc® M-710ic) directs a light beam from a laser head powered by a 3000-Watt class 4 solid-state Nd: YAG laser emitting at 1070 nm. model IPG YLS-3000-ST2. The HIGHYAG BIMO laser head is equipped with a variable zoom collimator and a fixed focusing lens. The assembly allows for circular focal spots ranging from 0.3 to 1.53 mm in diameter and a changeable welding speed. Also available are two optical fibers of 200 μm and 600 μm diameters. as shown in **Fig. 1.** Every two sheets of base metal were welded in a butt joint configuration by three types of beam oscillation (sinusoidal path. triangular path and square path). Therefore. a DC scanner was used to draw the three types of beam oscillation characterized by a constant amplitude of 1.5 mm and a constant frequency of 300 Hz. Several welds are performed by varying the laser power. the welding speed and the welding mode. The laser welding experiments were designed by the Taguchi method using an orthogonal L9 grating This design was chosen based on the variation of the main welding parameters. namely laser power. welding speed. and welding mode between ASTM A36 mild steel sheets. as shown in **Table 3**. which varies between three levels. The L-9 orthogonal array used for the laser welding tests is shown in **Table 4.**

Table 3. Process parameter levels

Process Parameters	**Symbol**	**Level 1**	**Level 2**	**Level** 3
Laser Power [W]	P	1800	2000	2200
Welding Speed [mm/s]	S	30	40	50
Oscillation Patterns	M	Sinusoidal	Triangular	Square

Table 4. Parameters used for the Taguchi method

Test	**Laser Power (W)**	**Welding Speed (mm/s)**	**Welding Pattern**
1	1800	50	Square
2	1800	40	Sinusoidal
3	1800	30	Triangular
4	2000	30	Sinusoidal
5	2000	50	Triangular
6	2000	40	Square
7	2200	40	Triangular
8	2200	30	Square
9	2200	50	Sinusoidal

2.3 Sample preparation

The welded samples were machined by a CNC machine. and cut by a benchtop dual-purpose abrasive machine. Three parts were used to measure tensile strength. and one part was made into polish-ready specimens using a multipurpose compression mounting press with a pressure of 4200 psi to measure microhardness. as shown in **Fig. 2.**

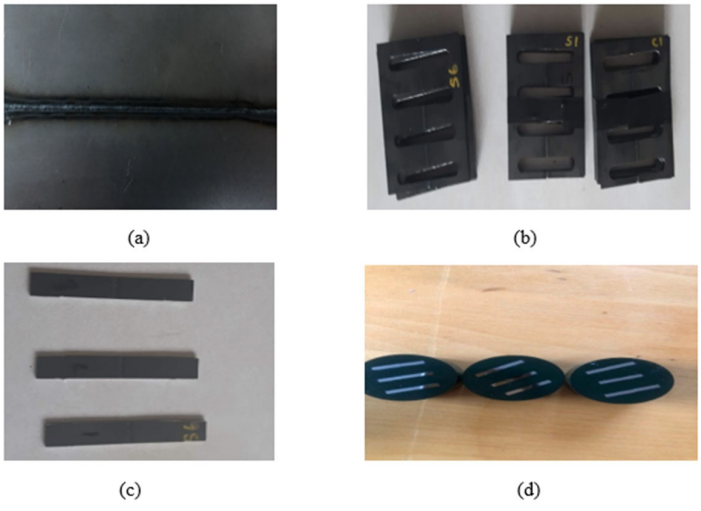

Fig. 2. The following figure shows (a) ASTM A36 steel plates after welding. (b) The two plates after machining. (c) Plates after cutting. (d) Mounted samples with epoxy

2.4 Micro-hardness analysis

Hardness measurements were performed using the Vickers microhardness technique (ST-2000) Fig. 3 (b). The polished samples were placed in the durometer to measure the microhardness in the region along the median plane of the weld (perpendicular section via the tool direction of the welded steel alloy plates. which was a measurement line 5 mm to the right and left of the center of the weld. as shown in **Fig. 3 (a)**. The load applied was 200 g for 10 s.

Fig. 3. The above figure shows (a) The line of hardness measurements (b) The Vickers microhardness tester (ST-2000)

2.5 Tensile test

The tensile test is the standard method for evaluating a material's mechanical integrity. Throughout the design process, the tensile test is frequently used to provide fundamental data on material strength as an acceptance test for material specification. The main parameter that describes the stress-strain curve obtained during the tensile test is tensile strength (UTS). yield strength (σy), modulus of elasticity (E), percent elongation (ΔL%), and area reduction (RA%) are all measures of plasticity. This method of testing can also be used to determine hardiness, resilience, and Poisson's ratio (v). In our study, we performed ASTM E8 tensile tests on welded specimens at room temperature using an MTS 810 testing machine and a testing speed of 0.025 mm/min, as described in **Fig. 4 (a)** and **Fig. 4 (b)**.

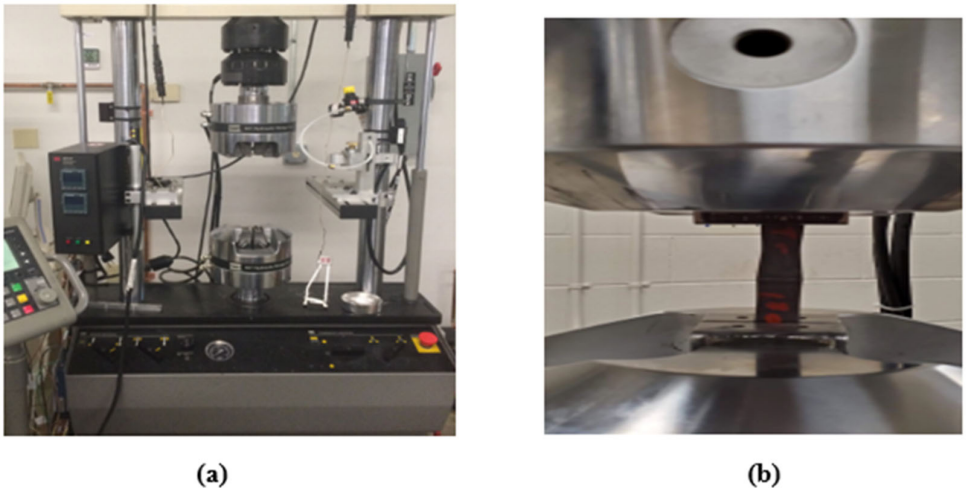

Fig. 4. Tensile test setup used for the experiments: (a) MTS 810 tensile machine. (b) specimen location during tensile testing

3. Results and Discussion

3.1 Hardness profile analysis

Fig. 5 shows the distribution of microhardness in the laser welding area for laser welding by three types of beam oscillations (sinusoidal. triangular and square) with the laser welding parameters (laser power and welding speed). For ASTM A36 steel. The hardness of the base metal is about 124 HV. The average micro-hardness of the weld fusion zone of the triangular pattern which is shown in Fig. 5 (b) is ≈ 260 Hv for the welding parameters; 1800 W. 30 mm/s. In addition. the same sample has an average value of ≈239 Hv in the weld zone with the welding parameters i.e., 2000 W. 50 mm/s as shown in **Fig. 5 (b)**. Furthermore. it can also be seen in **Fig. 5 (b)** that for the welding parameters; 2200 W. 40 mm/s. the weld zone depicts an average of ≈202 Hv. A similar trend can be observed for the sinusoidal and square patterns as shown in **Fig. 5 (a)** and Fig. 5 (c). In comparison. the average microhardness values of triangular pattern waves are higher for all the varying parameters as compared to sinusoidal and square patterns.

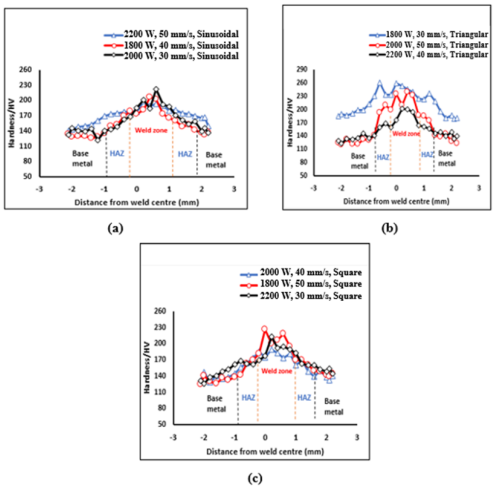

Fig. 5. The above figure shows the micro-hardness distributions for all the welded samples with different parameters: (a) Cross-section view of the welded joints indication of various zones (b) Square pattern (c) Triangular pattern (d) Sinusoidal pattern

3.2 Analysis of tensile properties

Transverse tensile properties such as ultimate tensile strength (UTS) were evaluated for each of the welded tests in the Taguchi L9 experimental design. The results obtained, which are the average of three measurements, are more trustworthy because three specimens were prepared and examined for each experimental series. The maximum stress-strain curves for all the testing in this investigation are displayed in **Fig. 7**. The elastic regions of the curves are not always the same height, as seen above, suggesting that Young's modulus is affected in the experiments. The results found are between (395.30-433.40) MPa. as shown in **Table 5**. Experiment cycle 9's parametric combination yields a weak tensile strength of 395.30MPa. In contrast, a maximum tensile strength of 433.40 MPa is calculated from the parametric combination of the third experimental cycle. Test 9's low tensile strength can be traced back to the significance of defects created during welding. The tensile samples' fracture trajectories show that the metal broke away from the melt zone and the heat-impacted zone, deep in the base metal. In a few cases, however, underfill and other faults likely caused the fracture to occur along the melt line. The fracture trajectory of the tensile samples after fracture shows that the fracture occurred mainly in the base metal. away from the melt zone and heat-affected zone but for a few samples, the fracture was produced in the melt line. probably due to defects such as underfill. As shown in **Fig. 6 (a)** and **Fig. 6 (b).**

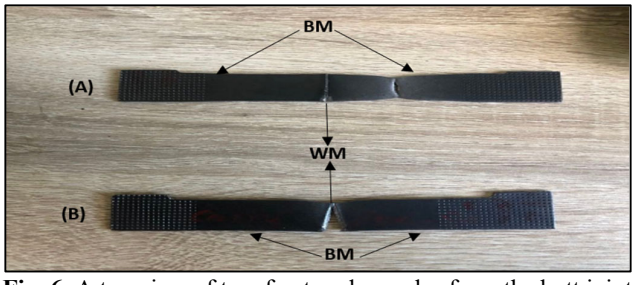

Fig. 6. A top view of two fractured samples from the butt joint tensile tests

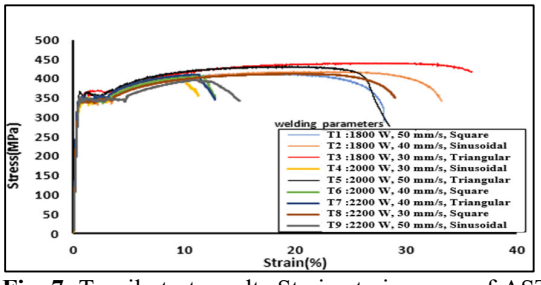

Fig. 7. Tensile test results Strain-strain curve of ASTM A36 mild steel

Table 5. Taguchi orthogonal L9 Design of experiment with tensile test results

S. No.	Laser Power (W)	Welding Speed (mm/s)	Pattern Type	UltimateTensile Strength (MPa)
1	1800	50	Square	412.02
2	1800	40	Sinusoidal	419.26
3	1800	30	Triangular	433.4
4	2000	30	Sinusoidal	405.13
5	2000	50	Triangular	430.02
6	2000	40	Square	409.37
7	2200	40	Triangular	411.54
8	2200	30	Square	409.95
9	2200	50	Sinusoidal	395.3

3.3 ANOVA analysis and development of the response surface (RS) regression model

Analysis of variance

The response surface model was created after analysis of variance (ANOVA) revealed the most influential input parameters and their interactions with the desired output. For this ANOVA study, we used the stepwise regression technique to get rid of the terms that weren't statistically significant. In this technical procedure, the probability value of each term in the analytical model is compared to a predetermined Fisher ratio. If the p-value (significant probability value) for an ANOVA term is less than the confidence level, then that term can be considered significant [9]. The developed model was given a 95% confidence level in this research. Since the terms were found to significantly affect the empirical relationships, "p-values" below 0.05 indicate significance. Table 6 displays the outcomes of a one-way analysis of variance (ANOVA) test conducted on UTS (tensile strength). The ANOVA analysis tables detail the efficient and significant input parameters for each response. The R2 value is used to check the fit between the predicted and measured data for all output responses, the R2 value was close to 100%. showing the strong correlation between the experimental and predicted results. The factors of welding by pattern and laser power have the greatest contribution worth 49.78% and 33.62% then the welding speed with less contribution equal to 1.82%. In the second step. We analyzed the effects of bidirectional interactions. we notice that the interaction (V*M) has an average contribution equal to 14.59%.

Table 6. ANOVA table for ultimate tensile strength

Variable	DDL	Square Sum	Contribution (%)	Mean Square	F-Value	P-Value
Power (W)	1	382.24	33.62	512.605	474.48	0.002
Speed (mm/s)	1	20.68	1.82	20.683	19.15	0.048
Pattern	2	565.91	49.78	64.349	59.56	0.017
Two-factor interaction: S*M	1	165.85	14.59	82.925	76.76	0.013
Error	2	2.16	0.19	1.08		
Total	8	1136.85	100			
S = 1.03940	R^2 = 99.81%	Adjusted R^2 = 99.24%	PRESS = 46.2553	R^2 (Pred) = 95.93%		

The final mathematical model determined by the above analysis is shown below in the following form:

Square Pattern: $UTS = 589.31 - 0.06536\ P - 1.2037\ S$ (1)

Sinusoidal Pattern: $UTS = 530.80 - 0.06536\ P + 0.1621\ S$ (2)

Triangular Pattern: $UTS = 536.32 - 0.06536\ P + 0.4846\ S$ (3)

As a diagnostic tool, the normal probability plot of the studentized residuals was crucial to illustrate, see **Fig. 8.** The residual plot looks like it's heading toward a straight line, so we know the normality assumption was met.

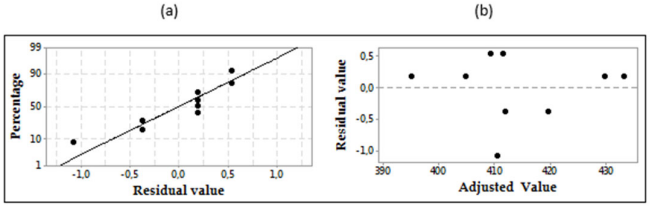

Fig. 8. The above figure shows (a) Normal probability residual (b) normal probability residual as a function of the fitted value

3.5 Variation of the developed model

In order to apply this model to predict and control the welding results, it is necessary to validate their fitting model. All 9 experimental runs had their predicted values computed and compared to their actual values, **Table 7** shows that.

Table 7
Variation of test results

S. No.	Laser Power (W)	Welding Speed (mm/s)	Pattern Type	Ultimate Tensile strength value (MPa)		Error (%)
				Experimental	Model	
1	1800	50	Square	412.02	411.47	0.13
2	1800	40	Sinusoidal	419.26	419.64	0.09
3	1800	30	Triangular	433.4	433.21	0.04
4	2000	30	Sinusoidal	405.13	404.94	0.05
5	2000	50	Triangular	430.02	429.83	0.04
6	2000	40	Square	409.37	410.44	0.26
7	2200	40	Triangular	411.54	411.91	0.09
8	2200	30	Square	409.95	409.41	0.13
9	2200	50	Sinusoidal	395.3	395.11	0.05

In addition, the error percentages in the prediction are in good agreement with the experimental results, demonstrating the developed models' accuracy. The validation curve of the model fit is presented in **Fig. 9**, respectively. According to the curve. the actual values are distributed along the diagonal line and close to the curve of the predicted values in most cases. indicating that the data are correct. predicted in most cases. indicating that the data fit is good.

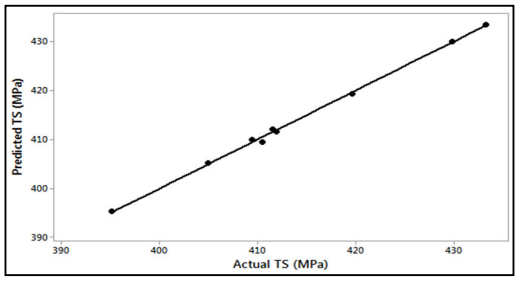

Fig. 9. Validation of the model fit

3.6 Effect and optimization of process parameters on tensile strength (UTS)

Interaction effects and surface plots

Three-dimensional (3D) contour and surface plots of weld strength as a function of process parameters during welding with three different types of laser beam oscillations are shown in **Fig. 10**. **Fig. 11** and **Fig. 12**. Weld strength is low when using a high laser power and a slow welding speed when welding with a sinusoidally oscillating laser beam, as shown in **Fig. 10 (a)** and **Fig. 10 (b).** As the laser power was reduced and the welding speed was slowed, more heat was introduced per unit of joint length increasing joint strength as a result of increased melting and mixing at the joint. The optimal weld strength can be achieved by choosing an appropriate combination of welding speed (45-50 mm/s) and laser power (1800 W). In **Fig. 11 (a)** and **Fig. 11 (b)**, we see how the tensile strength of a laser-beam weld varies as a function of the laser power and welding speed during triangular oscillation welding. It has been observed that the tensile strength increases with welding speed and decreases with laser power. By adjusting the welding speed (35-50 mm/s) and the laser power, the ideal weld strength can be attained (1800 W). **Fig. 12 (a)** and **Fig. (b)** illustrate the effects of laser power and welding speed, respectively, on the weld strength during square oscillation welding with a laser beam. The high tensile strength of the weld is seen at low welding speeds and low laser powers. Boosting both the laser's strength and welding rate weakens the weld's ability to withstand tension. To optimize the weld strength, an appropriate combination of welding speed and laser power can be selected at a given time. Laser power and welding speed can be selected at 1800-1900 W and 30-35 mm/s, respectively.

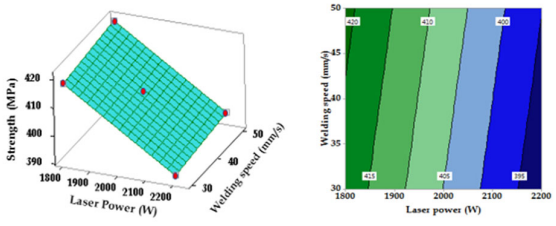

Fig. 10. Sinusoidal pattern (a) Contours plots (b) Response surface diagram showing the effect of 'P' and 'S' on the sinusoidal pattern weldment's tensile behavior.

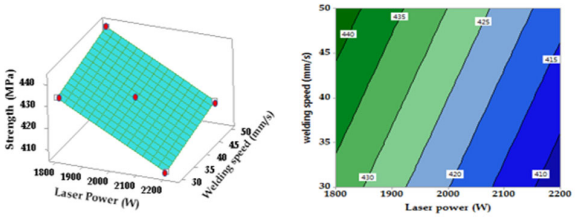

Fig. 11. Triangular pattern (a) Contours plots (b) Response surface diagram showing the effect of 'P' and 'S' on the triangular pattern weldment's tensile behavior.

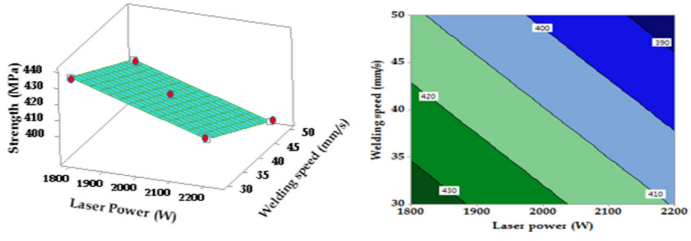

Fig. 12. Square pattern (a) Contours plots (b) Response surface diagram showing the effect of 'P' and 'S' on the square pattern weldment's tensile behavior.

The main effects graph shows a significant effect of laser power and welding mode on the UTS tensile strength. Indeed. We observe in **Fig. 13** that the decrease of the laser power during the laser welding by triangular oscillations causes a significant increase in the UTS tensile strength and the welding speed causes only a slight decrease in the UTS tensile strength value. **Fig.14** shows an interactive graph for the ultimate tensile strength. It can be concluded that the optimal setting for laser power. Welding speed and welding modes are 1800 W. 30 mm/s and a triangular oscillation of the laser beam. respectively.

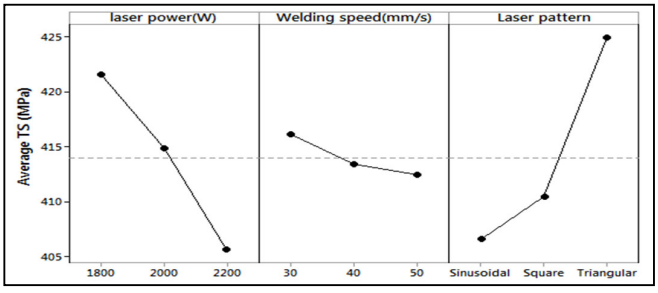

Fig. 13. Main effect curve of process parameters on tensile strength.

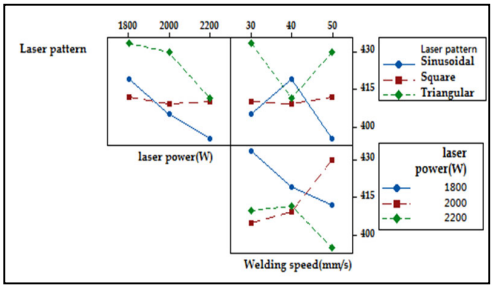

Fig. 14. Interaction graph of the input process parameters.

3.7 Optimization and confirmation of process parameters

Desirability functions, a function for determining the ideal response quality, have been used in RSM-based optimization procedures. The benefits of the desirability method include its ease of use, adaptability, and the ability to assign weight to each response. By employing the desirability approach to process optimization, the inherent nature of the response characteristics is reduced to a unidimensional factor known as the quality or desirability factor. This factor is between 0 and 1. In this part, we will try to zero in on the optimal settings for laser welding. The parameters for laser welding were fine-tuned using the desirability approach. The Minitab program provides a means of estimating the predicted values using a parameter, d, whose values range from 0 to 1 (with perfect values when d = 1) to acceptable values when d > 0.7. Our objective was to increase the UTS value to its fullest potential. The results of the optimization are shown in Fig. 15. The optimal welding conditions determined are the following: laser power interaction of 1800W. welding speed interaction of 50 mm/s and triangular oscillation of the laser beam. The expected response for the optimal combination is UTS=442.90 MPa with desirability of 1.

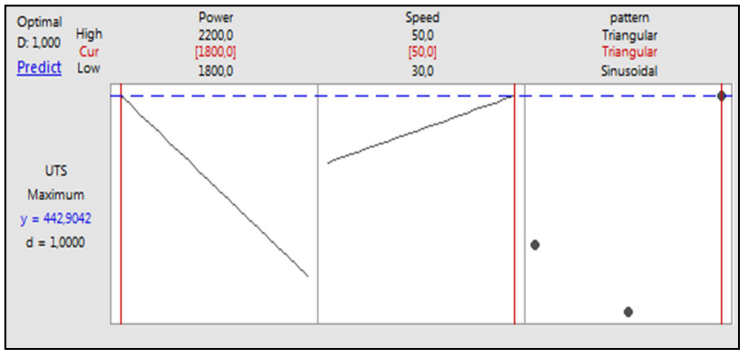

Fig. 15. UTS response optimization diagram

4. Conclusion

ASTM A36 mild steel materials were successfully laser welded using three types of laser beam oscillations and tested for tensile properties and microhardness measurements.

- The microhardness for all samples reaches its maximum in the fusion zone and gradually decreases from the fusion zone to the base metal. The maximum microhardness values for samples that were welded by triangular oscillation are higher than those that were welded by sinusoidal and square oscillations.
- The tensile strength during triangular oscillation welding of the laser beam is higher than those during sinusoidal and square oscillation welding.
- The optimal tensile strength during sinusoidal oscillation welding of the laser beam is a combination of 1800W for laser power and 45-50 mm/s for welding speed
- The optimal tensile strength during triangular oscillation welding of the laser beam is a combination of 1800W for the laser power and 35-50 mm/s for the welding speed

- The optimal tensile strength during square oscillation welding of the laser beam is a combination of 1800-1900W for the laser power and 30-35 mm/s for the welding speed
  the decrease in laser power during laser welding by the three types of oscillations causes a significant increase in the UTS tensile strength
- The most suitable combination of welding parameters was obtained. which is described as follows: the laser power is 1800 W. the welding speed is 30 mm/s and the welding mode is triangular

Data availability

The data is available upon request.

Disclosure Statement

There are no competing interests for this study.

References

Ancona, A., Lugarà, P. M., Sorgente, D., & Tricarico, L. (2007). Mechanical characterization of CO2 laser beam butt welds of AA5083. *Journal of Materials Processing Technology*, *191*(1–3), 381–384. doi: 10.1016/J.JMATPROTEC.2007.03.048

Benyounis, K. Y., Olabi, A. G., & Hashmi, M. S. J. (2008). Multi-response optimization of CO2 laser-welding process of austenitic stainless steel. *Optics & Laser Technology*, *40*(1), 76–87. doi: 10.1016/J.OPTLASTEC.2007.03.009

Bhadra, R., Pankaj, P., Biswas, P., & Dixit, U. S. (2019). Thermo-Mechanical Analysis of CO 2 Laser Butt Welding on AISI 304 Steel Thin Plates. *International Journal of Steel Structures*, *19*(1), 14–27. doi: 10.1007/s13296-018-0085-z

Çam, G., Yeni, Ç., Erim, S., Ventzke, V., & Koçak, M. (2013). Investigation into properties of laser welded similar and dissimilar steel joints, *3*(4), 177–189. doi: 10.1179/STW.1998.3.4.177

Cao, R., Han, C., Guo, X., Jiang, Y., Liao, F., Yang, F., Dou, G., Yan, Y., & Chen, J. (2022). Effects of boron on the microstructure and impact toughness of weathering steel weld metals and existing form of boron. *Materials Science and Engineering: A*, *833*, 142560. doi: 10.1016/J.MSEA.2021.142560

Cheng, H., Zhou, L., Li, Q., Du, D., & Chang, B. (2021). Effect of welding parameters on spatter formation in full-penetration laser welding of titanium alloys. *Journal of Materials Research and Technology*, *15*, 5516–5525.

Derevyagina, L. S., Gordienko, A. I., Orishich, Malikov, A. G., Surikova, N. S., & Volochaev, M. N. (2020). Microstructure of intercritical heat affected zone and toughness of microalloyed steel laser welds. *Materials Science and Engineering: A*, *770*, 138522. doi: 10.1016/J.MSEA.2019.138522

El-Batahgy, A.-M., Khourshid, A.-F., & Sharef, T. (2011). Effect of Laser Beam Welding Parameters on Microstructure and Properties of Duplex Stainless Steel. *Materials Sciences and Applications*, *02*(10), 1443–1451. doi: 10.4236/MSA.2011.210195

Gao, M., Zeng, X., Yan, J., & Hu, Q. (2008). Microstructure characteristics of laser–MIG hybrid welded mild steel. *Applied Surface Science*, *254*(18), 5715–5721. doi: 10.1016/J.APSUSC.2008.03.070

Geng, Y., Akbari, M., Karimipour, A., Karimi, A., Soleimani, A., & Afrand, M. (2019). Effects of the laser parameters on the mechanical properties and microstructure of weld joint in dissimilar pulsed laser welding of AISI 304 and AISI 420. *Infrared Physics & Technology*, *103*, 103081.

Karakizis, P. N., Pantelis, D. I., Dragatogiannis, D. A., Bougiouri, V. D., & Charitidis, C. A. (2019). Study of friction stir butt welding between thin plates of AA5754 and mild steel for automotive applications. *The International Journal of Advanced Manufacturing Technology*, *102*, 3065–3076.

Kumar, P., & Sinha, A. N. (2018). Microstructure and mechanical properties of pulsed Nd:YAG laser welding of st37 carbon steel. *Procedia Computer Science*, *133*, 733–739. doi: 10.1016/J.PROCS.2018.07.125

Pankaj, P., Tiwari, A., Bhadra, R., & Biswas, P. (2019). Experimental investigation on CO2 laser butt welding of AISI 304 stainless steel and mild steel thin sheets. *Optics and Laser Technology*, *119*(November 2018), 105633. doi: 10.1016/j.optlastec.2019.105633

Prabakaran, M. P., & Kannan, G. R. (2019). Optimization of laser welding process parameters in dissimilar joint of stainless steel AISI316/AISI1018 low carbon steel to attain the maximum level of mechanical properties through PWHT. *Optics & Laser Technology*, *112*, 314–322.

Satpal, S., Bhopale, A., Deshpande, P., & Athawale, A. (2020). Fabrication of ZnO-functionalized polypyrrole microcomposite as a protective coating to enhance anticorrosion performance of low carbon mild steel. *Journal of Applied Polymer Science*, *137*(4), 48319.

Wang, J. (2019). Determination of dimensional profile and heat input of welded joints with average temperature. *International Journal of Precision Engineering and Manufacturing*, *20*, 651–662.

Wang, P., Chen, X., Pan, Q., Madigan, B., & Long, J. (2016). Laser welding dissimilar materials of aluminum to steel: an overview. *The International Journal of Advanced Manufacturing Technology*, *87*, 3081–3090.

Xia, M., Tian, Z., Zhao, L., & Zhou, Y. N. (2008). Metallurgical and Mechanical Properties of Fusion Zones of TRIP Steels in Laser Welding. *ISIJ International*, *48*(4), 483–488. doi: 10.2355/ISIJINTERNATIONAL.48.483

Yang, J., Oliveira, J. P., Li, Y., Tan, C., Gao, C., Zhao, Y., & Yu, Z. (2022). Laser techniques for dissimilar joining of aluminum alloys to steels: A critical review. *Journal of Materials Processing Technology*, *301*, 117443.

Zhang, M., Chen, G., Zhou, Y., & Liao, S. (2014). Optimization of deep penetration laser welding of thick stainless steel with a 10 kW fiber laser. *Materials & Design*, *53*, 568–576. doi: 10.1016/J.MATDES.2013.06.066